Reduction of the Gibbs Oscillation in Spectral Model Simulations

A. NAVARRA

Program in Atmospheric and Oceanic Sciences, Princeton University, Princeton, New Jersey

W. F. STERN AND K. MIYAKODA

GFDL/NOAA, Princeton University, Princeton, New Jersey

(Manuscript received 2 August 1993, in final form 14 December 1993)

ABSTRACT

Spectral atmospheric general circulation models (GCMs) have been used for many years for the simulation and prediction of the atmospheric circulation, and their value has been widely recognized. Over the years, however, some deficiencies have been noticed. One of the major drawbacks is the inability of the spectral spherical harmonics transform to represent discontinuous features, resulting in Gibbs oscillations. In particular, precipitation and cloud fields present annoying ripple patterns, which may obscure true drought episodes in climate runs. Other fields, such as the surface winds along the Andes, are also plagued by the fictitious oscillations. On the other hand, it is not certain to what extent the large-scale flow may be affected. An attempt is made in this paper to alleviate this problem by changing the spectral representation of the fields in the GCM. The technique is to apply various filters to reduce the Gibbs oscillations. Lanczos and Cesaro filters are tested for both one and two dimensions. In addition, for two-dimensional applications an isotropic filter is tested. This filter is based on the Cesaro summation principle with a constraint on the total wavenumber. At the end, two-dimensional physical space filters are proposed that can retain high-mountain peak values. Two applications of these filters are presented.

In the first application the method is applied to the orography field by filtering out sharp gradients or discontinuities. The numerical results with this method show some improvement in the cloud and precipitation fields, along with some improvement of the surface wind pattern, resulting in an overall better simulation.

In the second application, a Gibbs reduction technique is applied to the condensation process. In this paper the moist-adiabatic adjustment scheme is used for the cumulus parameterization, in addition to large-scale condensation. Numerical results with this method to reduce Gibbs oscillations due to condensation show some improvement in the distribution of rainfall, and the procedure significantly reduces the need for negative filling of moisture. Currently, however, this approach is only partially successful. The negative moisture areas at high latitudes can be, to some extent, controlled by an empirical procedure, but the filter approach is not sophisticated enough to satisfactorily remove the complex Gibbs oscillations present in the condensation field.

1. Introduction

It has been known since the inception of the spectral transform method (Orszag 1970; Eliasen et al. 1971; Bourke 1972) that some problems may arise when the spectral projection is used to represent fields with sharp spatial gradients or "discontinuities." These are known as Gibbs oscillations, associated with the transformation of the truncated spectral representation to physical space (Korner 1990; Lanczos 1956; Canuto et al. 1988). It consists of considerable (in some cases) oscillations in the vicinity of the discontinuity (see Fig. 1). Hoskins (1980) discussed the consequences of spectral truncation on the orography field. He proposed a filter to alleviate Gibbs oscillations based on a convolution approach, but his result did not receive widespread attention at that time, because it was not clear that Gibbs oscillations could lead to serious errors in the simulation. Other filters have been discussed by Hogan and Rosmond (1991).

Recently there has been renewed interest in the problem of Gibbs oscillations (hereafter referred to as the G bias) associated with errors in the simulation of the El Niño–Southern Oscillation. The simulated annual cycle of sea surface temperatures in the eastern equatorial Pacific has a serious bias in several models; errors in surface winds may be a contributing factor. It has been hypothesized (Miyakoda et al. 1993) that the G bias, generated by the steep Andes orography, plays an essential role in causing spurious surface winds. Motivated by this speculation, an approach similar to that used by Hoskins (1980) has been pursued—that is, applying a convolution operator to the spherical harmonic expansion of the orography. There is a wide range of choices for the convolution operator, which is essentially a filter. The filters make the ap-

Corresponding author address: Dr. Antonio Navarra, IMGA-CNR, Via Emilia Est 770, Modena, Italy.

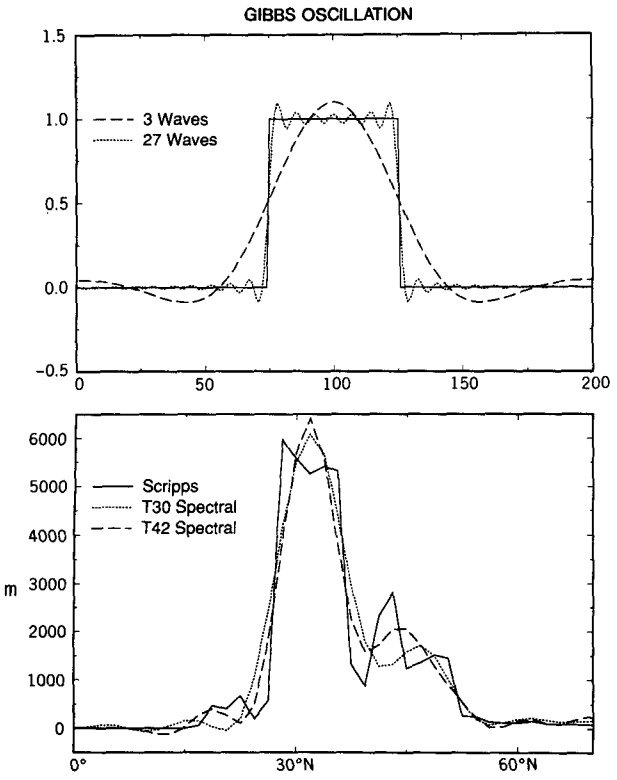

FIG. 1. Examples of the Gibbs oscillation. Top: a mathematical case of the square mountain. Bottom: a latitudinal section at 90°E through the Himalayas; the original orography data are provided by Scripps Oceanographic Institution. In both panels, spectrally represented orographies truncated at T30 and T42 are shown.

proximation more uniform by artificially damping the high-wavenumber part of the spectrum. However, when the fictitious components of high wavenumbers are eliminated, some significant fraction of low-wavenumber components are also lost. One of the problems addressed in this paper is how to handle this situation. With regard to the mathematical description of the G bias, there are many references in literature to one-dimensional filters (Canuto et al. 1988; Cai et al. 1992). Another issue to be addressed in this paper is a new class of generalized filters suitable for spherical harmonic representation; they will be tested in the context of general circulation model (GCM) simulations.

There are other components of the spectral GCM that have the potential for being affected by the G bias. In the standard formulation of spectral GCMs, physical processes are computed on the Gaussian grid, and their contribution to the tendencies is transformed back to spectral space. If sharp gradients are present, the G bias is introduced. Prime candidates are physical processes that tend to produce relatively small-scale, highly discontinuous tendencies. Among them, the condensation of water vapor is a strong candidate because of its highly discontinuous nature. These convolution operators are tested by applying them to the tendency obtained from the condensation parameterizations.

In this paper, a background account of two problems associated with the G bias is given in section 2. The mathematical theory of the G bias is described in section 3, and numerical examples are presented in sections 4 and 5. Some special remarks on the oscillation in the finite-difference calculations and the physical space filter are given in section 6.

2. Background

a. Problems related to orography

On a sphere for the spherical harmonics case, the G bias comes from two sources. The first one is from the Fourier transform for longitude, and it is especially large in the vicinity of north–south mountain ranges, such as the Andes. The second comes from the Legendre transform for latitude, and it is particularly evident near mountain ranges extending east–west, such as the Transantarctic Mountains.

The top panel of Fig. 1 shows the G bias for the idealized case of step orography (solid line). Direct approximations are made with 3 and 27 terms (waves) in the truncated Fourier series. The bias is seen as a series of oscillations that result in a nonuniform approximation of the original function. This problem is seen not only in the vicinity of the discontinuity, but also far from it. The oscillation overshoots the jump with an overestimation of about 10%. The increase of resolution does not improve the situation; the increase of wave components reduces the scale of the oscillations but leaves the overshooting unchanged.

A mechanism similar to the step mountain described above is also found in a realistic mountain. The bottom panel of Fig. 1 shows a latitudinal section of the earth's orography at 90°E (solid line, marked as Scripps); this longitude is dominated by the Himalayas as the major profile. Mathematically speaking, in this case Legendre rather than Fourier coefficients are involved, but the result is similar. This section is particularly suited for demonstrating the G bias because of the unique shape that resembles the step mountain in the upper panel. The spectrally transformed orography, either at T30 or T42 resolution (triangular truncation at wavenumber 30 or 42, respectively), show fictitious oscillations. The spurious positive oscillation in the center of the high plateau creates a higher maximum than in the original mountain. Similar oscillations can be noted in other locations (top panels of Figs. 2–3); they exhibit an almost textbook appearance of the bias for Fourier series, as is seen over the eastern Pacific Ocean off the Peruvian coast (Fig. 3). The G bias manifests itself as a well-defined train of oscillations that extends into the ocean nearly as far as the date line. A similar situation can be seen at higher resolution (i.e., T42; Fig. 4). In this case, a more detailed profile of the overall moun-

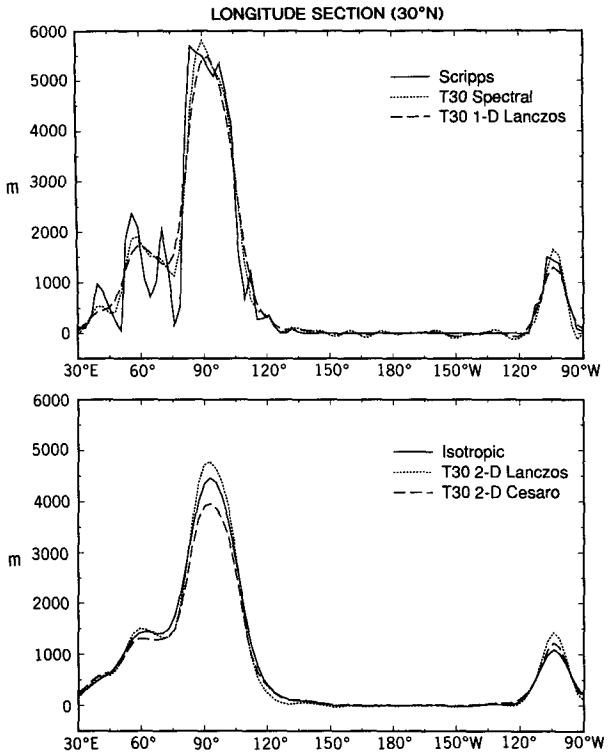

FIG. 2. The 20°S longitudinal profiles of orography from Fourier series T30. Top: the unsmoothed together with the 1D Lanczos-filtered orography. Bottom: the Gibbs-reduced orographies using the 2D Lanczos, the 2D Cesaro, and the isotropic filters.

tains can be reproduced, but the oscillations are still visible.

Nonetheless, it has been generally believed that the spurious oscillations caused by the G bias would have a minimal impact on atmospheric model simulations. Once these oscillations occur, the model would simply adjust to the large-scale orography, leaving a small-scale error associated with this unavoidable feature of the spectral representation. In reality, however, it is not difficult to find examples in which the effect of the bias is far from negligible. For example, substantial errors are produced in the low-level meridional wind in our GCM. We will investigate this point and demonstrate that the effect is found not only in the low-level wind field, but also in other variables, such as clouds and precipitation. Figure 5 shows a section of the meridional component of the wind v at 850 hPa along 20°S. The top panel shows the observations for the years 1980–87, based on the analyses of ECMWF (European Centre for Medium-Range Weather Forecasts), as compiled by Schubert et al. (1990), and the bottom is obtained from our 8-yr integration of the model in the spectral GCM described in Stern and Miyakoda (1991) truncated at triangular 30, with 18 vertical levels (T30L18). Though some agreement is noticeable, the model solution seems to oscillate at a higher spatial frequency than the observations. At around 60°W the meridional wind undergoes larger oscillations [amplitude O(5 m s^{-1})] in the longitudinal direction that are not seen in the observations. Smaller amplitude fluctuations are also evident between 10°E and 160°W. The location of the main error corresponds closely to the area of the largest G bias (Fig. 3, top). Because of the steep gradient due to the Andes, the untreated orography has a major bump just off the coast. Furthermore, the orography oscillations remain substantial as they extend into the Pacific Ocean.

To summarize, though it is not certain that the wind error is positively due to the G bias, the G bias cannot be ignored and some care must be taken to treat it properly.

b. Problems related to condensation

The second application of filtering involves the condensation of moisture. It is well known that spectral transform models have difficulty in maintaining the positive definite character of tracer fields, including water vapor (Gordon and Stern 1982). Another source of negative mixing ratio is the condensation process, which takes place in the physical space, generating spotty and noisy fields of moisture. The spectral transform of such a field, which contains many kinks and steep gradients, will be strongly affected by the G bias.

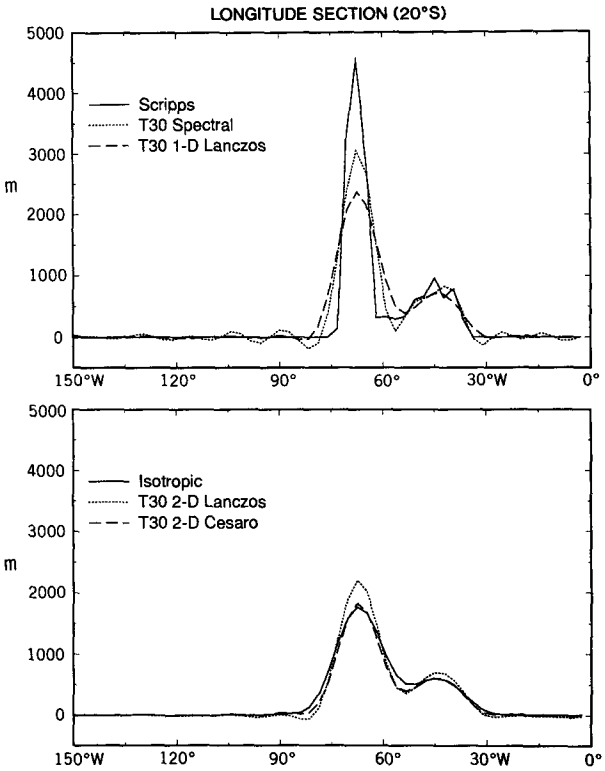

FIG. 3. The 30°N longitudinal profiles of orography from T30 Fourier series. See the caption of Fig. 2 for further explanation.

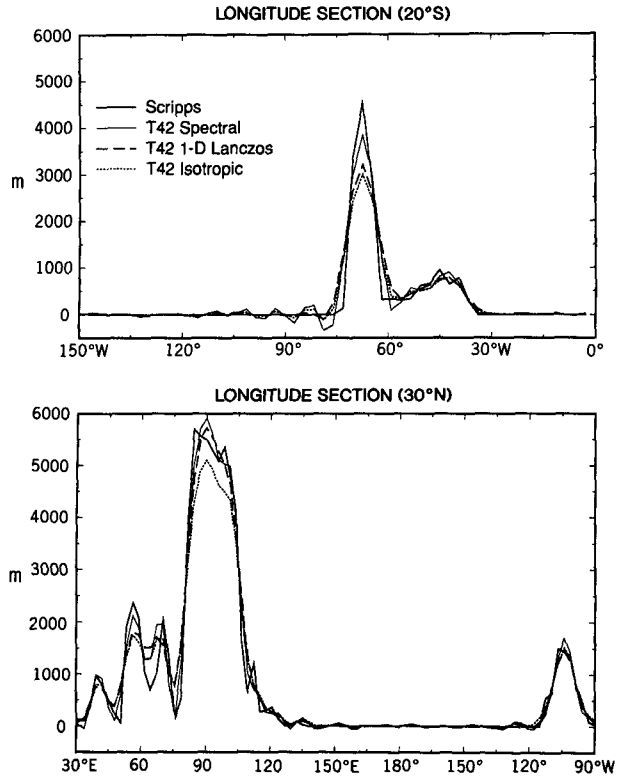

FIG. 4. The same as Figs. 2 and 3 except by T42.

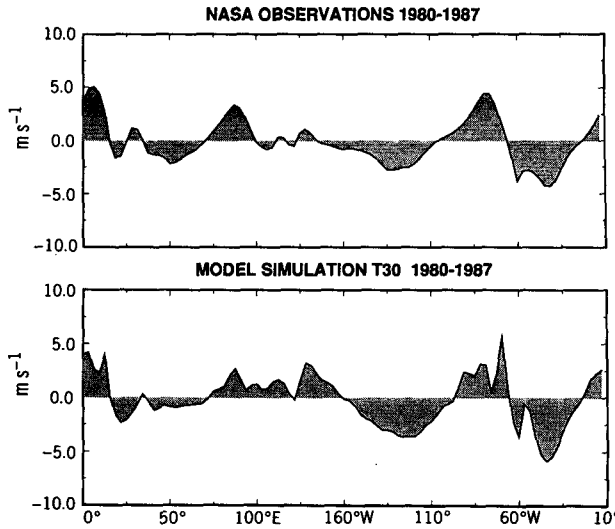

FIG. 5. The 20°S longitudinal profiles of meridional component of wind v at 850 hPa. Top: from the NASA atlas of 1980–1987 ECMWF analysis, Schubert et al. (1990). Bottom: the same field from the T30 8-yr simulation.

Condensation can occur sometimes at just a single grid point, causing great variability in the moisture field. This kind of noise may be minimized if condensation operates at many grid points at the same time, which is often the case in the Tropics. On the other hand, at higher latitudes, condensation occurs at relatively isolated spots, and therefore, many kinks are created in the moisture and temperature fields, including the holes of moisture. These holes are conventionally filled by borrowing moisture from nearby locations. The error is further aggravated by the G bias when the transform calculation is applied to the new moisture field. The G bias will create its own oscillations that will adversely affect the convection process. Significant errors associated with this perverse combination have been largely overlooked.

Another disturbing feature probably associated with the G bias is the large amount of high spatial wavenumber activity in the model cloud field (Gordon 1992). Although the cause has not been precisely determined, it is clearly locked in phase with topographic features, suggesting a delicate interplay between orographic and water vapor G bias.

One can better appreciate the potential problem by looking at a typical increment field for moisture. Figure 6 shows the time rate of change in the moisture field at about 900 hPa produced by the condensation processes, which have been averaged over a month. The field is negative definite since the mixing ratio can only decrease due to condensation. The gridpoint pattern, computed on the Gaussian grid of the model (Fig. 6,

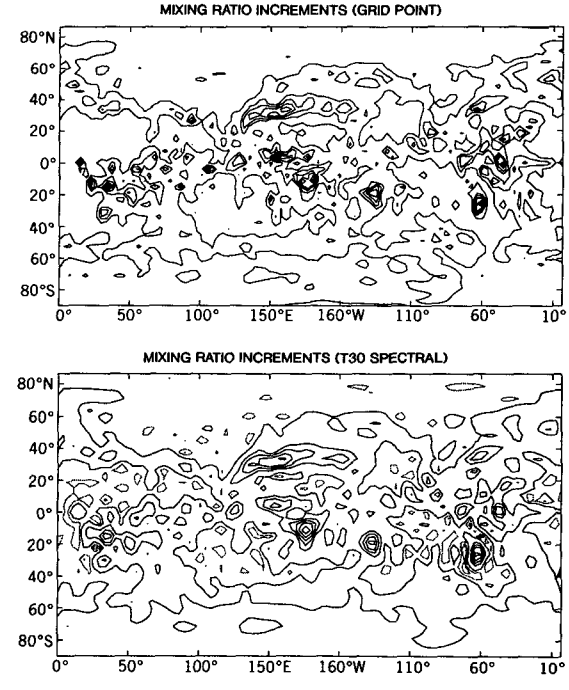

FIG. 6. Time tendency in mixing ratio of water vapor averaged over a month of a GCM integration. Top: the gridpoint field. Bottom: spectrally truncated at T30. The sign convention is such that solid contours indicate a negative change in water vapor content due to condensation. Solid lines are at −0.5, −1, −2, −3, −4, −5, −6, and −7, and dashed contours are at 0.01 and 0.05 [10^{-3} g(kg)$^{-1}$ d^{-1}].

top), exhibits a complex pattern, with several small intense features. The bottom panel of Fig. 6 shows the result of a triangular spectral transform at T30. The distribution in the bottom panel, originally computed on the grid by the condensation parameterizations, is the result of transforming by the pseudospectral model. A clear signature of the G bias is visible. It is even more worrisome since it distorts the negative definite character of the increment. When this moisture field is used subsequentially, the G bias will show up as a fictitious source of moisture.

3. Techniques to reduce the Gibbs oscillations

In order to correct the G bias, a filtering procedure is applied to the harmonic coefficients for the spectral representation of the orography or the moisture distribution. There are several one-dimensional filters for the Fourier transform, the Lanczos filter being one of the most popular techniques. For two-dimensional problems, double transformations are required—that is, Fourier transform over longitudes and Legendre transform over latitudes. For the Legendre transform, filters similar to the Lanczos are not known.

a. One-dimensional filters

In finite numerical mathematics, a function $f(x)$ is represented by a finite number $2N + 1$ of Fourier harmonics:

$$f_N(x) = \sum_{k=-N/2}^{N/2} \hat{f}_k e^{ikx}. \quad (1)$$

The partial sum f_N converges to f as $N \to \infty$ point by point, but if the function contains some discontinuities (e.g., the square function in the top panel of Fig. 1), the convergence in the maximum norm is not guaranteed. The maximum value of f_N over the interval ($\max(f_N)$) will not converge to $\max(f)$, and oscillations of magnitude about 10% of the amount of the jump appear in the vicinity of the discontinuity. Increasing N results only in moving the wiggles closer to the location of the jump.

In the idealized situation of Fig. 1, there exists no N large enough to accurately resolve the gradient. On the other hand, in the case of a steep but finite gradient, a resolution exists at which the Gibbs oscillation disappears completely. However, numerical results show that this limit has not been reached at T42 resolution in our case (Fig. 7 and Fig. 9). In reality, the situation is further complicated by the two different transforms that are necessary on the sphere; it is practically impossible to reach the resolution that eliminates the G bias completely.

The traditional remedy to the G bias is using a convolution kernel that improves the convergence rate of the Fourier series for large N. In practice, Eq. (1) is substituted with

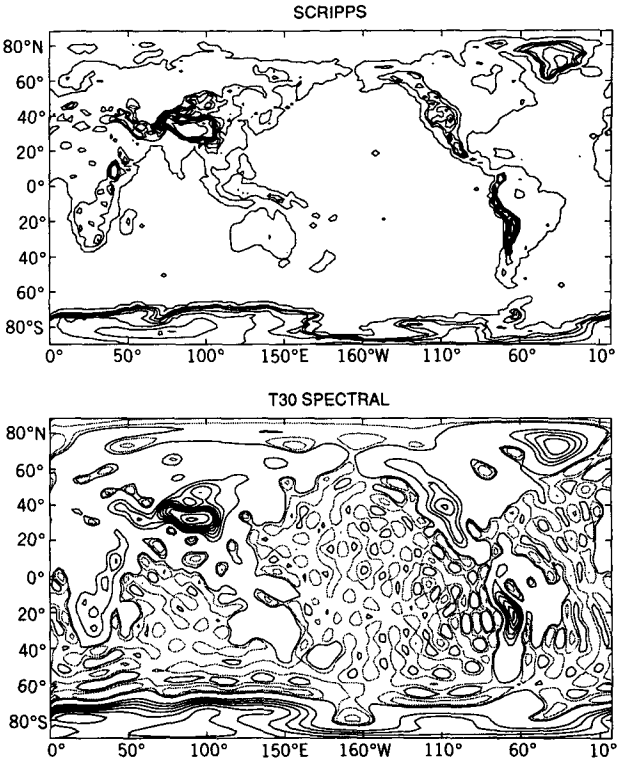

FIG. 7. Orography. Top: Scripps gridpoint data. Bottom: the spectral T30 resolution. Dashed contours are at −300, −100, and −10, and solid contours are at 50, 1000, 1500, 2000, 2500, 3000, 3500, 4000, 5000, and 6000 m.

$$f_N(x) = \sum_{k=-N/2}^{N/2} \hat{\sigma}_k \hat{f}_k e^{ikx}, \quad (2)$$

where the $\hat{\sigma}_k$ are suitably chosen factors. Canuto et al. (1988) list some of the most widely used filters, such as the Cesaro or Lanczos kernel. The Cesaro filter is also known as the Bartlett filter (Jenkins and Watts 1968). In general, they eliminate the oscillations at the cost of spreading the jump and losing some amplitude. The Lanczos filter (Lanczos 1956),

$$\hat{\sigma}_k = \frac{\sin 2k\pi/N}{2k\pi/N} \quad \text{for} \quad k = -N/2, \cdots, N/2, \quad (3)$$

and the Cesaro filter,

$$\hat{\sigma}_k = 1 - \frac{|k|}{(N/2 + 1)} \quad \text{for} \quad k = -N/2, \cdots, N/2, \quad (4)$$

are chosen as two options for application in this paper. Hereafter, they are referred to as 1D Lanczos and 1D Cesaro, 1D indicating one dimensional.

b. Two-dimensional filters

The simplest attempt to reduce the G bias of a 2D field is to apply a 1D filter, Lanczos or Cesaro for ex-

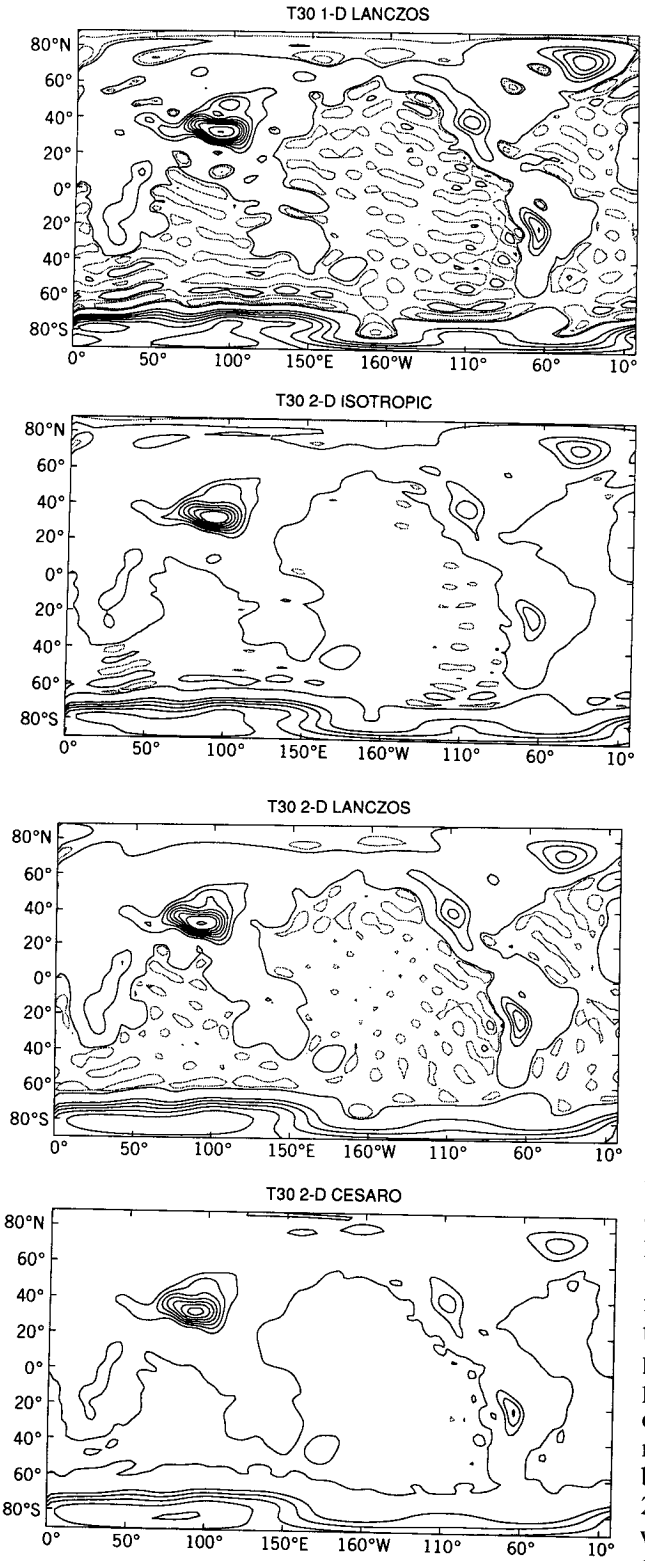

FIG. 8. As in Fig. 7 except the spectrally filtered orography at T30. Top: the 1D Lanczos filter. Second: the 2D isotropic filter. Third: the 2D Lanczos filter. Bottom: the 2D Cesaro filter. Contour interval is the same as in Fig. 7.

ample, to the Fourier coefficients one dimensionally at each latitude (Duchon 1979). This approach is only marginally effective in eliminating the oscillations in two dimensions (see later Fig. 8, top and Fig. 9, middle), although it may be adequate for certain purposes. This treatment causes a small but noticeable distortion of the features in the zonal direction. Another undesirable consequence of using only a one-dimensional Fourier filter on the sphere is that it organizes the oscillations in coherent bands oriented east–west. The transforms involving Legendre polynomials are not immune from the G bias. This effect may be seen over the periphery of Antarctica in the bottom panel of Fig. 7 and the top panel of Fig. 9; the ripples are quite evident.

It is therefore necessary to investigate the possibility of a two-dimensional filter. Let a variable Z defined over a sphere be expressed as (see, e.g., Bourke 1972)

$$Z(\phi, \lambda) = \sum_{m=-M}^{M} \sum_{n=|m|}^{N} Z_n^m P_n^m(\cos\phi) e^{im\lambda}, \quad (5)$$

where (ϕ, λ) are latitude and longitude, P_n^m is a Legendre polynomial, Z_n^m are the spherical harmonic coefficients of Z, m is the zonal wavenumber, and n is the degree of Legendre function or the two-dimensional wavenumber for the spherical harmonics. Terms N and M are truncation parameters. Here $N = |m| + J$ specifies the order of truncation, where J is an arbitrary integer specifying a general form of truncation; rhomboidal truncation ($N = |m| + M$) and triangular truncation ($N = M$) are common types of truncation.

A simple 2D filter can be obtained by the extension of the 1D filters, Lanczos or Cesaro. In other words, the weights defined in (3) or (4) are applied to the Fourier and Legendre coefficients equally, ignoring the fact that the Legendre wavenumbers are not Fourier wavenumbers. The resulting filters will be referred to, in this paper, as 2D Lanczos and 2D Cesaro, respectively. These simple filters are effective, but they retain a strong smoothing, and they do not guarantee shape preservation of the horizontal features.

A desirable property for this study is that two-dimensional features are treated equally in both longitudinal and latitudinal directions. The filters should preserve this property as much as possible. As was pointed out by Sardeshmukh and Hoskins (1984), in order to achieve this objective it is necessary to formulate filters that depend only on the total wavenumber of the spherical harmonics, n. For example, the 2D Lanczos filter does not belong to this category, whereas the Bessel function filter (Thompson 1956) or the one that will be described below does belong to this category.

A filter with the desired shape-preserving characteristics and with more sound mathematical foundation is based on the Cesaro summation principle. This is a

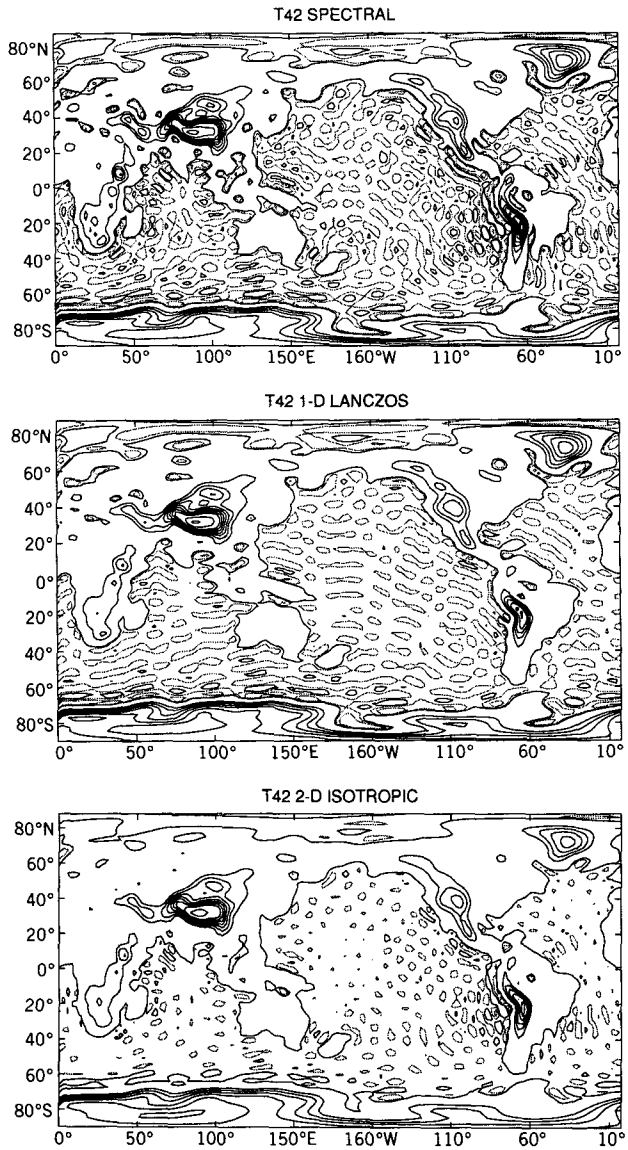

FIG. 9. Spectrally filtered orography at T42 resolution. Top: the original T42. Middle: 1D Lanczos filter. Bottom: The 2D isotropic filter. See the caption of Fig. 8a for further explanation.

well-known technique to improve convergence of series. Given a series $\sum_{i=0}^{K} a_i$, the Cesaro summation substitutes the series by the arithmetic means of the partial sums $1/(K+1)\sum_{k=0}^{K} R_k$, where the partial sum is defined as $R_k = \sum_{i=0}^{k} a_i$.

In the case of (5), the partial sums are defined as

$$R_l = \sum_{m=-M}^{M} \sum_{n=|m|}^{l} Z_n^m P_n^m(\cos\phi) e^{im\lambda}, \qquad (6)$$

where the limit l can be for either a rhomboidal or a triangular truncation. One can show that R_l in (6) conforms to the partial sum $P_k = \sum_{i=0}^{k} a_i$ in the Cesaro summation as follows. The formula (6) in the case of triangular truncation and $l < M$, for example, is transformed by changing the order of summation with respect to n and m as

$$R_l = \sum_{n=0}^{l} \Big[\sum_{m=-n}^{n} Z_n^m P_n^m(\cos\phi) e^{im\lambda} \Big].$$

Thus, $Z(\phi, \lambda)$ in (5) can be written as

$$Z(\phi, \lambda) = \frac{1}{N+1} \sum_{l=0}^{N} R_l$$

$$= \sum_{l=0}^{N} \sum_{m=-M}^{M} \sum_{n=|m|}^{l} \sigma_n^m Z_n^m P_n^m(\cos\phi) e^{im\lambda}. \qquad (7)$$

Note that in the case of the triangular truncation, $N = M$, and in the case of the rhomboidal truncation, $N = |m| + J$, in Eq. (7), in the same way as Eq. (5).

The coefficient of the filter σ_n^m has an expression in the triangular truncation case, for example, as follows: $Z(\phi, \lambda)$ in (7) can be expressed by a diagram summation with respect to n and m, writing symbolically the coefficient Z_n^m as (n, m); then Eq. (7), multiplied by $(N+1)$, is written as

$$\begin{aligned}(N+1)Z(\phi,\lambda) &= (0,0) + \begin{bmatrix}(1,0)(1,1)\\(0,0)\end{bmatrix} \\ &+ \begin{bmatrix}(2,0)(2,1)(2,2)\\(1,0)(1,1)\\(0,0)\end{bmatrix} + \cdots \\ &+ \begin{bmatrix}(N,0)\cdots\cdots(N,N-1)(N,N)\\\cdots\cdots\cdots\cdots(N-1,N-1)\\\quad\vdots\\(1,0)(1,1)\\(0,0)\end{bmatrix}.\end{aligned} \qquad (8)$$

The first term on the right-hand side of (8) represents $(n = 0, m = 0)$; the second term represents $(n = 0, m = 0)$, $(n = 1, m = 0)$, and $(n = 1, m = 1)$, etc. In (8), only the terms of $m \geq 0$ are written, omitting the terms of $m < 0$. Equation (8) is then regrouped, according to the same coefficients, as

$$(N+1)Z(\phi,\lambda) = (N+1)(0,0) + N[(1,0),(1,1)] + \cdots + [(N,0),(N,1)\cdots(N,N)]. \qquad (9)$$

Dividing (9) by $N+1$, one obtains

$$Z(\phi,\lambda) = (0,0) + \frac{N}{N+1}[(1,0),(1,1)] + \cdots + \frac{1}{N+1}[(N,0),(N,1)\cdots(N,N)]. \qquad (10)$$

This is rewritten in a compact form, using the summation notation, as

$$Z(\phi, \lambda) = \sum_{m=-M}^{M} \sum_{n=|m|}^{N} \left(1 - \frac{n}{N+1}\right)(n, m).$$

Thus, the equation that is valid both for the triangular and rhomboidal truncations is given by

$$Z(\phi, \lambda) = \sum_{m=-M}^{M} \sum_{n=|m|}^{N} \sigma_n^m Z_n^m P_n^m(\cos\phi) e^{im\lambda}, \quad (11)$$

where, for the triangular case,

$$\sigma_n^m = 1 - \frac{n}{N+1}, \quad (12)$$

and for the rhomboidal case,

$$\sigma_n^m = \begin{cases} 1 - \dfrac{|m|}{N+1}, & n = |m|, \cdots, 2|m|; \\ 1 - \dfrac{n-|m|}{N+1} & n = 2|m|, \cdots, N. \end{cases} \quad (13)$$

The filters based on this method satisfy the isotropic requirement—that is, they depend only on the total wavenumber n, irrespective of triangular or rhomboidal truncation. They will subsequently be referred to as the 2D isotropic filter. Hereafter in this paper a triangular truncation will be used exclusively.

Apart from these filters, another family of filters has been proposed. They are exponential forms, which are designed empirically. These filters do not have a mathematical basis, as σ_n^m in (12) or (13), and therefore they are known as pseudodifferential operators. These exponential filters can be written as

$$\sigma_n^m = \exp[-\alpha(n/N)^{2\beta}], \quad (14)$$

where $\alpha = 32$ and $\beta = 2$, 4, or 8 are usually used. Note that exponential filters corresponding to ∇^{-4} operators have been used by Hoskins (1980) to reduce the G bias, but they severely smooth the mountain ranges.

c. *Application of the filters to orography*

For the purpose of this paper we will use box-averaged mountains in a 1° × 1° quadrangle, known as the "Scripps orography," compiled by Gates and Nelson (1975).

The top panel of Fig. 7 shows the original grid orography from Scripps, while the bottom panel shows the direct (without filter) application of T30 spectral representation. The maps of the spectral orography (Fig. 7, bottom) show an annoying pattern of oscillations, fanning out from the main mountain ranges in the east–west direction, as in the case of the Andes and the Rockies, or in the north–south direction, as in the case of the Transantarctic Mountains and the Himalayas. Fictitious negative values of about 600 m are reached in the eastern Pacific, and values of about 200 m below the mean sea level are common.

The Gibbs reduction procedure (subsequently referred to as G reduction) removes the spurious oscillations, though the highest mountain peaks are lowered somewhat. The effects of using the 1D Lanczos and the 2D isotropic filter are shown in Fig. 8 for T30 resolution. The only one-dimensional filter tested in this paper is the Lanczos filter (1D Lanczos). Predictably, a simple application of the 1D Lanczos filter to the east–west component of orography turns out to be insufficient to correct the north–south components. Since little is known about correcting the G bias on a two-dimensional sphere, several filters are tested. The isotropic filter is very effective, though it reduces amplitude to some extent. Figure 8 shows the orographies processed by the 2D Lanczos and 2D Cesaro filters.

Figure 9 shows the mountains at higher spectral truncation (i.e., the T42). The oscillations are still quite noticeable, particularly in the eastern Pacific, where a large erroneous depression of O(600 m) is located west of the Andes. Elsewhere the errors are smaller, but in general errors of O(200 m) are visible on the entire globe. Consistent with the G bias theory, the depression associated with the Andes is of the same order of magnitude in the T42 orography as in the T30. As is speculated, higher resolution will not automatically eliminate the G bias, and it gives rise to an artificial amplification of the oscillations (see the bottom panel of Fig. 1). It is evident that the isotropic filter keeps the mountain isotropic, while the 1D filter introduces a zonal bias.

The behavior of the filters is summarized in the diagram of Fig. 10 in terms of the maximum and minimum values of the filtered and unfiltered orography over the globe for the two resolutions. Black circles

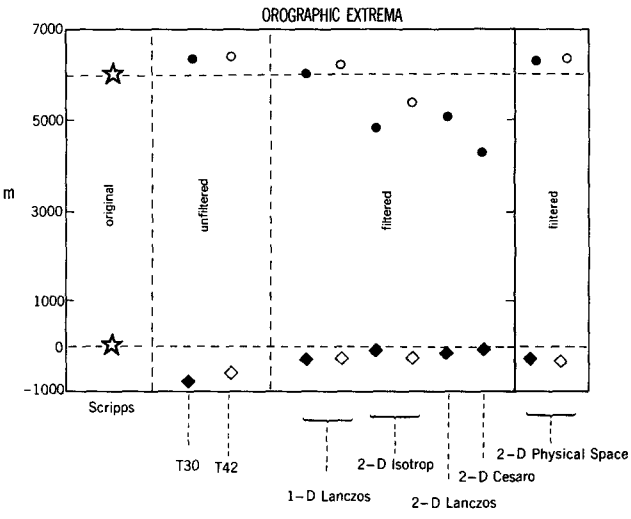

FIG. 10. Global maxima and minima of orographies, which are processed by various filters discussed in the text. The circles and diamonds represent maxima and minima, respectively. Solid and hollow symbols refer to the T30 and T42 Fourier series, respectively. Scripps indicates the original gridpoint mountain.

and diamonds correspond to the T30 resolution, while hollow circles and diamonds correspond to the T42 resolution. The spectral truncation is producing errors in the maximum and minimum mountain heights over the globe at both truncations T30 and T42. The spectrally truncated fields overestimate the absolute values of both *minimum and maximum* values, and the error does not necessarily improve with a higher resolution, as the maximum error is larger at T42 than at T30. Higher mountains per se are not necessarily more realistic. The filters are very effective in removing the negative dips, but the smoothing effect is also evident.

The filters at the right end of Fig. 10, noted by a 2D physical space filter, will be discussed in section 6b. To summarize section 3, the 2D isotropic filter appears to be satisfactory in the case of the high-resolution model, but in the case of the low-resolution model, the peaks of the Himalayas, for example, are appreciably lowered. This filter will be used in the next section.

4. Experiments involving orography

In this study, a spectral GCM triangularly truncated at zonal wavenumber 30 (i.e., T30) with 18 vertical levels (Gordon and Stern 1982; Gordon 1992) is used. The effect of the G-reduced orography on GCM simulations is investigated by comparison with a control experiment using the original orography (see the top panel of Fig. 3 and Fig. 7). The G-reduced orography is treated by applying the 2D isotropic filter and is shown in Figs. 3 and 8. The G-reduced experiment uses the same parameter settings as that of the control experiment, except for the mountains. Both experiments perform 8-yr simulations from 1981 to 1987. The results are presented for the winter and summer season defined as December, January, February (DJF) and June, July, August (JJA) averages.

It is worthwhile to mention here that to compensate for the deficiency of the G bias a correction is applied to the sea surface temperature in the model solution. The procedure, adopted in several spectral models, modifies the SST according to the local terrain height using the adiabatic lapse rate, trying to avoid heat sources at unrealistic altitudes. The mechanism is still active in the G-reduced experiments, but becomes a minor effect once the G bias has been removed.

Returning to the orography experiment, it is shown that there is a definite impact of the new orography. The wind fields, precipitation, clouds, and soil wetness fields are markedly better organized and exhibit more realistic scales. On the other hand, the upper air fields are relatively less affected by the new orography.

The impact is most pronounced in the precipitation pattern. Figure 11 presents precipitation patterns for JJA. The comparison is made among three distributions—that is, the control, the G-reduced orography, and the observed climatology based on Jaeger (1976). The ripples generated by the Andes and the Transantarctic Mountains have been dramatically reduced. Another clear improvement in the G-reduced case can be seen in the rainfall over the Sahel—namely, the transformation of an unrealistic spotty precipitation over central Africa into a large-scale pattern. The last point is particularly important for the study of Sahel drought, because noisy rainfall may mask the simulation of drought. The Southeast Asia precipitation appears to be worse. It is conceivable that the monsoonal circulation might have been adversely affected by the smoothing of the Himalayas.

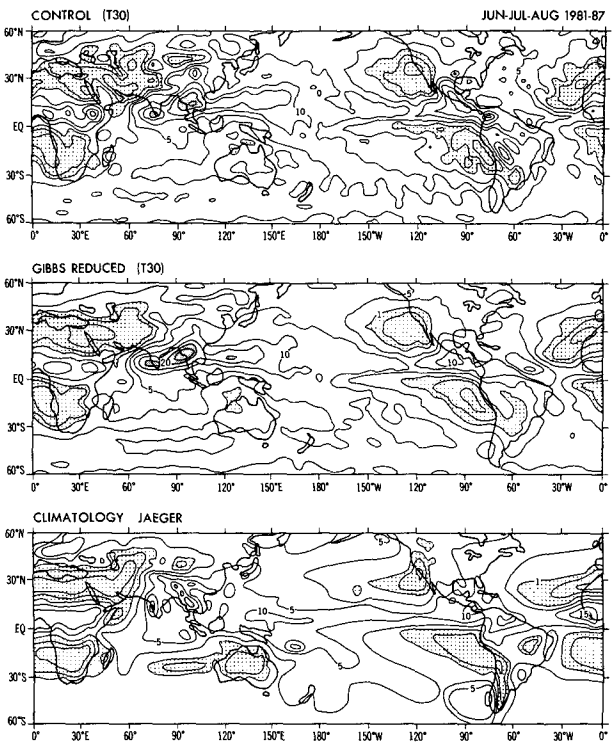

FIG. 11. Rate of precipitation for JJA, averaged for 7 yr from the 1981–87 model simulations (top and middle), and for the observed climatology (bottom) compiled by Jaeger (1976). Contours are: 20, 15, 10, 5, 2.5, 1.0, 0.5, and 0 mm day^{-1}.

Figure 12 displays the divergence fields at 850 hPa for the 7-yr average. Ripples along the Andes, Antarctica, the Rockies, and the Himalayas are conspicuous in the control, whereas they are suppressed by the G-reduced experiment. This effect may have a substantial impact on the El Niño process in the eastern Pacific. The top, middle, and bottom panels in Fig. 13 compare the meridional components of upper-level wind v at the 200-hPa level. The impact of smoother mountains on this variable is expected to be much less than other variables at lower levels, and yet the effect is clearly noticeable. In fact, the G-reduced orography appears to give better results overall, but some adverse effect shows up as a weakening of the stationary waves over the Rocky Mountains. It is difficult to assess the absolute performance of the simulations, but the main

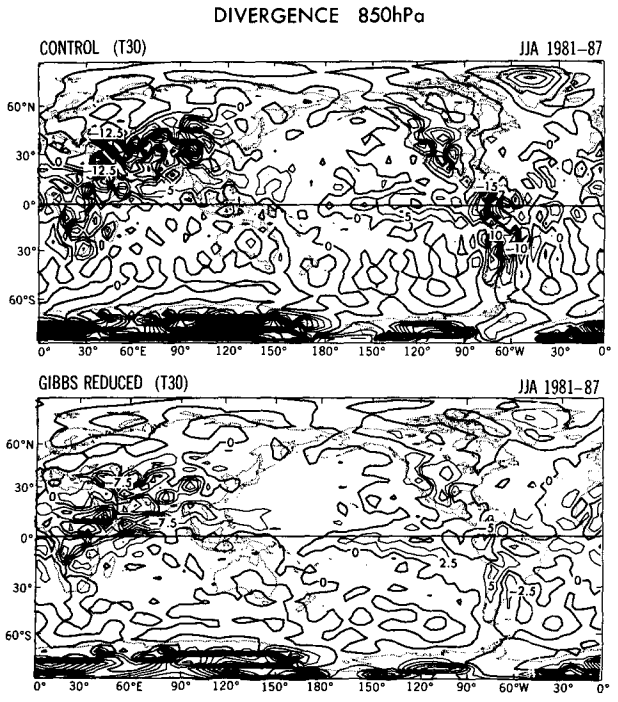

FIG. 12. Divergence of wind at 850 hPa for JJA, averaged over 7 yr. Top: the control. Bottom: the G reduced. Contour interval is 2.5 $\times 10^{-6}$ s^{-1}.

point of the comparison is to show that no traumatic degradation of the simulation occurs because of the mountain smoothing.

The total cloud field is shown in Fig. 14. The unrealistic ripples present in the control (top panel) are generally absent without the G bias. The clouds are more spatially coherent in the G-reduced experiment (bottom panel). A more detailed investigation reveals that most of the improvement comes from the low cloud field that was substantially affected by the G bias, whereas the high clouds are relatively less sensitive.

Finally the top, middle, and bottom panels in Fig. 15 show the standing eddy components of geopotential height at 300 hPa—that is, $z_e = z - \langle z \rangle$, where Z is the height, and $\langle z \rangle$ is the zonal average. The simulated eddies in the control and the G-reduced runs agree well with the observation. There was some concern that the smooth mountains might tend to produce weaker eddies, but here the intensity of eddies in the G-reduced case appears to be almost the same as that in the control.

5. Experiments involving condensation

In this application, we expect a more difficult situation than in the orography applications. The number, location, and strength of discontinuities in the moisture distribution are unknown a priori, and they vary during the course of integration. In this paper, we will use the moist convective adjustment as the cumulus parameterization (Manabe et al. 1965), which may help to create negative moisture. This is in addition to the so-called large-scale condensation. Other convection schemes such as Kuo or Arakawa–Schubert create the same problem. In this situation, the G bias makes things even worse.

A possible remedy is to remove the G bias from the moisture and temperature fields. In practice, after allowing condensation to take place, the spectral field is modified by applying the G-reduction filter to the moisture and temperature fields. This process is performed every time step. In this way amplification of the G bias caused by the spectral transform will be minimized. Here we will illustrate the experiments conducted so far. Three versions are tested as follows:

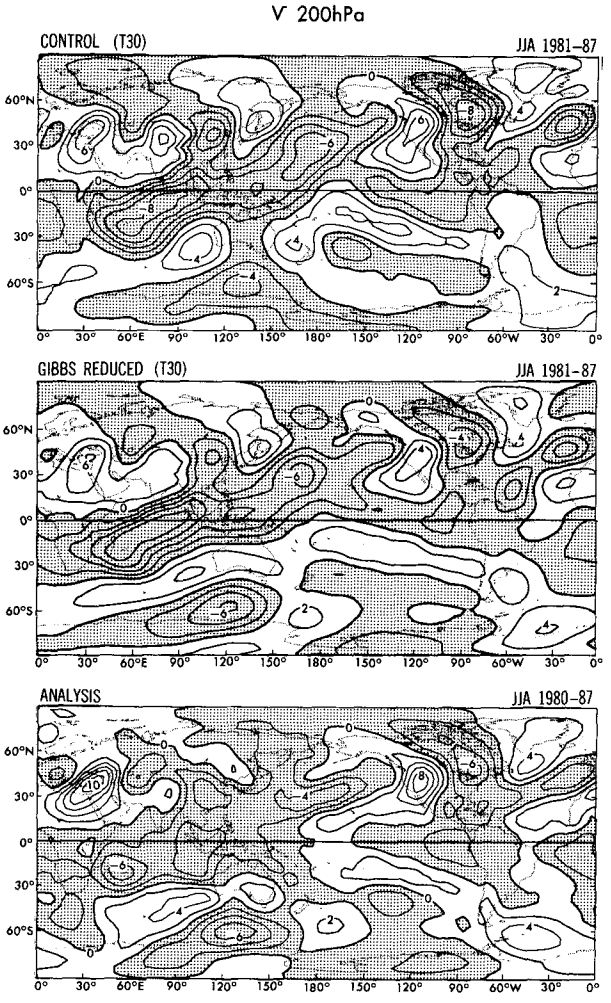

FIG. 13. Meridional component of wind at 200 hPa for JJA, averaged over 7 yr. Top: the control; middle: the G reduced; and bottom: ECMWF analysis averaged over 8 yr. Contour interval is 2 m s^{-1}. The negative regions are stippled.

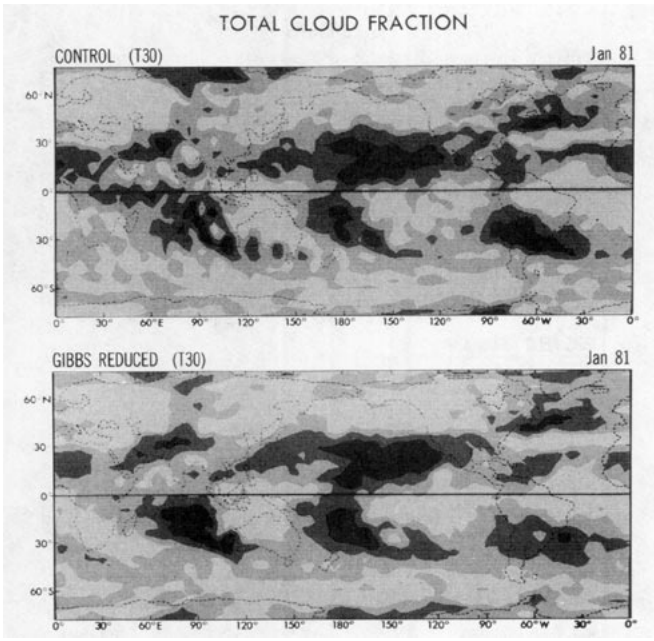

FIG. 14. Total cloud field, averaged for January 1981. Top: the control experiment. Bottom: the G-reduced experiment. Progressively lighter shading indicates cloud fraction cover n_s where $0 \leq n_s \leq 0.2$, $0.2 \leq n_s \leq 0.4$, $0.4 \leq n_s \leq 0.6$, and $n_s \geq 0.6$, respectively.

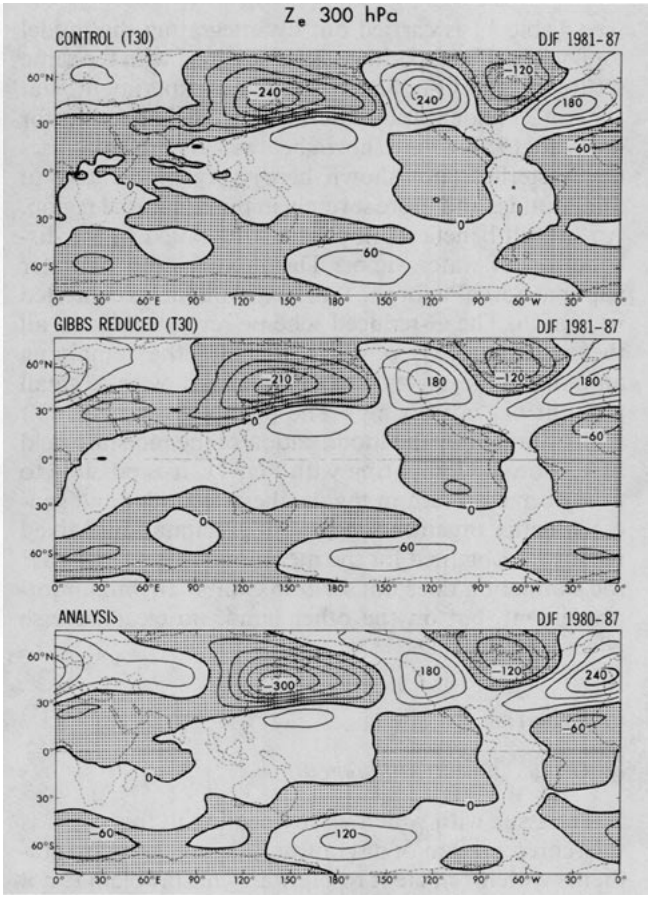

FIG. 15. Geopotential height eddies at 300 hPa for DJF, averaged over 7 yr (m). The eddy is the deviation from its zonal mean.

- version 1—the 1D Lanczos filter is applied to the total components of temperature and mixing ratio of water vapor;
- version 2—the 1D Lanczos filter is applied at each latitude alone, applying it to the total mixing ratio only if some negative values are detected at some longitudes; and
- version 3—the isotropic filter is applied to the time increment (time change) of mixing ratio and temperature.

Several short experiments were performed to evaluate the three versions. In experiments with version 1 and 2, the negative areas of moisture disappear completely. However, the impact of G reduction in version 1 on the overall GCM solution is excessively large, so that the simulation is not acceptable. The action of the filter is too indiscriminate, and the large-scale components of temperature are damaged, resulting in the loss of a realistic equator–pole gradient and a rapidly deteriorating simulation.

On the other hand, the results of version 2 are better. In this case, the filter is applied at individual latitudes to the mixing ratio, but only if negative values are detected at any longitude along that particular latitude. The constraint limits the filter almost exclusively to the polar latitudes and to the higher levels, and it seems rather efficient in removing the negative ones.

Another approach was taken for version 3. In this case the filter was applied to the incremental part of temperature and mixing ratio after the condensation parameterization. Results reveal that the negative areas are not totally eliminated, possibly because of other sources of G bias in the model. For example, the dynamical stretching of a water vapor tongue may give rise again to the G bias. However, it is still true, as version 2 shows, that the filter is capable of reducing the G bias in the water vapor distribution. In the case of version 2, there is a small problem in justifying the apparent inconsistency of not applying the filter to temperature, but only to water vapor. One may consider it not as a physical process, but only as an ad hoc numerical device.

Based on the results of the short experiments, an experiment of G-reduced mountain and water vapor

TABLE 1. Experiments for the G-reduced orography.

Experiment	Description
Control	Standard orography, bottom of Fig. 7
G-reduced mountain	2D isotropic filter (T30L18), bottom of Fig. 8
G-reduced mountain and water vapor	2D isotropic filter (T30L18)

(see Table 1) is carried out by integrating the model for 8 years. The experiment was designed with the same setting as the G-reduced mountain experiment, but version 2 condensation filtering is used. The results for the years 1981–87 are shown below. Version 2 increases the westerlies (not shown here) very moderately in midlatitudes and more severely in the equatorial region. An overall beneficial impact can be noted in the distribution of water vapor. The mixing ratio of water vapor at 850 hPa for the three experiments is exhibited in Fig. 16. The G-reduced scheme removes almost all the negative areas of moisture, and the remaining amount of negatives can be removed with a small amount of "borrowing." The precipitation (Fig. 17) is also affected by the modification of the moisture field in version 2. Comparing with Fig. 11, it is possible to note decreased rain in the northern latitudes and generally better organized regions of precipitation. Mixed results are obtained for the meridional wind (Fig. 18); the simulation does not seem to exhibit any major improvement, but on the other hand, no clear adverse effect is noticeable.

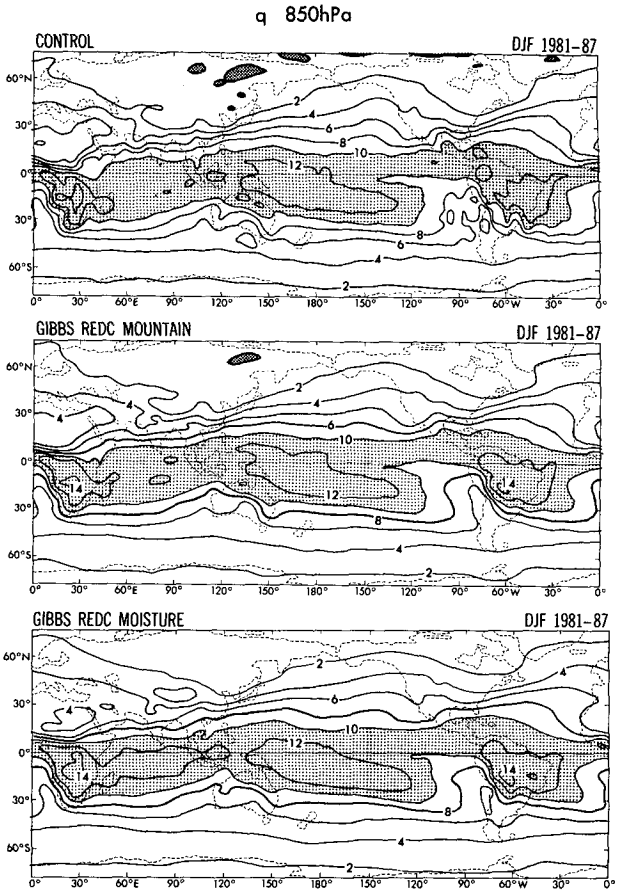

FIG. 16. Mixing ratio of water vapor at 850 mb for the control experiment (top), G-reduced mountains (middle), and G-reduced mountains and moisture (bottom) (see Table 1). Contour interval is 2.0 g kg^{-1}.

6. Remarks

a. G bias in finite differencing

The issue with which we are dealing in this paper is the representation of discontinuities and/or sharp gradients with insufficient resolution. This problem is not a prerogative of spectral models. In fact, all discretized equations suffer from the same type of problem. A finite-difference scheme would have similar difficulties in representing steep mountains as does the spectral transform method. One reason that this may not be evident is that the most popular differencing schemes include a substantial amount of implicit smoothing. The following example may be useful in clarifying this point. Assume we compute the derivative of the function f in (1). The exact derivative in spectral space, truncated at N, is

$$\frac{df_N}{dx} = \sum_{k=-N/2}^{N/2} ik\hat{f}_k e^{ikx}. \tag{15}$$

The finite-difference approximation to (15), using a centered second-order accurate scheme with a grid interval Δx can be written as

$$\begin{aligned}\frac{df_N}{dx} &\approx \sum_{k=-N/2}^{N/2} \hat{f}_k \left[\frac{e^{ik(x+\Delta x)} - e^{ik(x-\Delta x)}}{2\Delta x}\right] \\ &= \sum_{k=-N/2}^{N/2} \hat{f}_k i e^{ikx} \left[\frac{\sin(k\Delta x)}{\Delta x}\right] \\ &= \sum_{k=-N/2}^{N/2} \hat{f}_k i k e^{ikx} \left[\frac{\sin(k\Delta x)}{k\Delta x}\right]; \end{aligned} \tag{16}$$

since $\Delta x = 2\pi/N$, this equation shows that a Lanczos filter is applied implicitly by the differencing scheme. Higher-order schemes would obtain a weaker implicit filtering, resulting in a less and less effective smoothing. A fourth-order scheme, for instance, will obtain a filter of the form

$$\frac{1}{3}\left[\frac{\sin(2k\pi/N)}{2k\pi/N}(4 - \cos 2k\pi/N)\right].$$

Figure 19 shows the implicit filtering for a second- (dashed) and fourth- (solid) order differencing scheme. Improving the accuracy of the scheme (fourth order) would result in a less severe smoothing, and therefore, the G bias will start to appear.

Using this concept, one can develop the so-called polar filter for a gridpoint model. The filter has the characteristic of the isotropy and the smooth transition from the middle latitudes to the polar regions. For the latter purpose, the idea of the physical space filter, which will be described in the next subsection, is used.

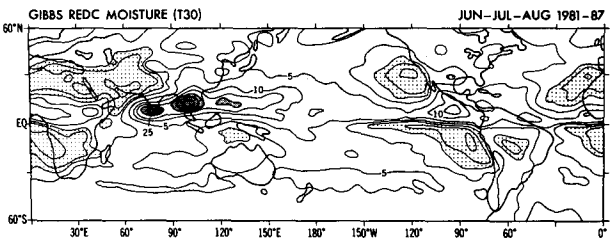

FIG. 17. Rate of precipitation for JJA, averaged over 7 yr, for the mountain and moisture G-reduced case (see Table 1). Contours are the same as in Fig. 11.

b. *Physical space filter*

Although the filters are far from being perfect, they can give reasonable results if information on the location of the "discontinuity" is available. The orographic G bias is probably affecting the entire mountain field in the same way, but it is generally regarded as having the most serious consequences over the oceans. In this case, fictitious ripples are obviously unrealistic, and there is potential for generating large errors. Therefore, it would be desirable to have a "selective" filter that would strongly eliminate the G bias over the oceans and, to a lesser extent, over the land. To construct such a physical space filter we start from the filtered spectral expansion in Eq. (5):

$$Z_N(\phi, \lambda) = \sum_{m=-M}^{M} \sum_{n=|m|}^{N} Z_n^m \sigma_n^m P_n^m(\cos\phi) e^{im\lambda}, \quad (17)$$

where the σ_n^m are the filter components, and the Z_n^m can be obtained from

$$Z_n^m = \int_0^{2\pi} \int_0^{\pi} Z(\lambda', \phi') P_n^m(\cos\phi') e^{-im\lambda'} d\phi' d\lambda'. \quad (18)$$

Substituting (18) into (17) we get

$$\begin{aligned} Z_N(\phi, \lambda) &= \sum_{m=-M}^{M} \sum_{n=|m|}^{N} \int_0^{2\pi} \int_0^{\pi} Z(\lambda', \phi') P_n^m(\cos\phi') \\ &\quad \times e^{-im\lambda'} d\phi' d\lambda' \sigma_n^m P_n^m(\cos\phi) e^{im\lambda} \\ &= \int_0^{2\pi} \int_0^{\pi} K(\phi, \phi', \lambda, \lambda') Z(\lambda', \phi') d\phi' d\lambda', \quad (19) \end{aligned}$$

where

$$K(\phi, \phi', \lambda, \lambda') = \sum_{m=-M}^{M} \sum_{n=|m|}^{N} \sigma_n^m P_n^m(\cos\phi) \times P_n^m(\cos\phi') e^{im\lambda} e^{-im\lambda'} \quad (20)$$

is the kernel of the filtered transform.

The kernel can be computed numerically from the Fourier and Legendre transforms. We can write Eq. (19) in finite mathematics assuming discrete longitudes and latitudes as indexes:

$$(z_N)(\phi, \lambda) = \sum_{\phi', \lambda'} K_{\phi\lambda\phi'\lambda'} z(\phi', \lambda'),$$

where it is possible to see that the kernel is a set of coefficients depending on four indexes. At each location $(\phi_0\lambda_0)$ the multiplication of the coefficients $K_{\phi\lambda\phi'\lambda'}$ with the field z will result in the truncated value of z at the grid point $(\phi_0\lambda_0)$, $(z_N)(\phi_0\lambda_0)$.

In practice the coefficients can be computed by choosing a special form of fields and performing a direct and reverse spherical transform. If we choose $z = \delta_{\phi\phi_0}\delta_{\lambda\lambda_0}$, namely a function that is equal to one at $(\phi_0\lambda_0)$ and zero elsewhere, then we can see that

$$(z_N)(\phi, \lambda) = \sum_{\phi'\lambda'} K_{\phi\lambda\phi'\lambda'} \delta_{\phi'\phi_0} \delta_{\lambda'\lambda_0} = K_{\phi\lambda\phi_0\lambda_0}.$$

Repeating the calculation for all $(\phi_0\lambda_0)$ will complete the computation of the coefficients.

The kernel in Eq. (20) contains the effect of the transform and the filter when it is applied to the gridpoint field Z. We now have a tool to apply the filter in physical space rather than in spectral space. Applying the kernel to each grid point of the Scripps orography, one can reproduce the filtered orography that has been obtained previously, but now there is freedom in applying the filter selectively to a local domain. We take as the gridpoint field the spectrally truncated field at the bottom panel of Fig. 7 and treat it with the filtered kernel in selected locations.

Figure 20 shows the effect of applying such a filter only to the ocean and negative altitude points (according to a land–sea mask at T30) of the spectrally truncated T30 orography and applying a standard spectral transform again. The oceanic ripples have been virtually eliminated, reducing them to less than −10 m, and only a tiny spot of about 100 m has been left close to South America and north of Antarctica. The main mountain ranges have been left untouched: the Himalayas maximum is at about 6000 m (see 2D

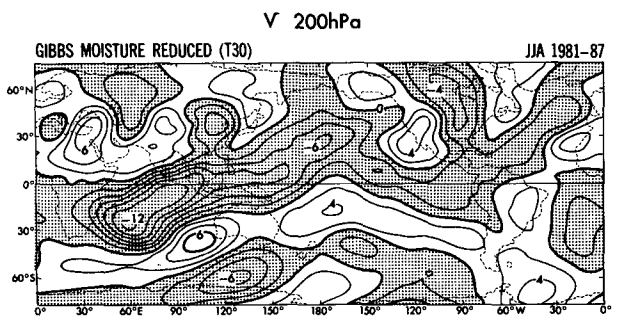

FIG. 18. Meridional component of wind at 200 hPa for JJA, averaged over 7 yr for the mountain and moisture G-reduced experiment. Contour interval is 2 m s^{-1}.

physical space filter in Fig. 10); the Rockies are at 2500 m; and the Andes reach 3000 m. In this particular case, an exponential filter [see Eq. (14)] with $\alpha = 32$ and $\beta = 2$, combined with a Vandeven filter of order 2 (Vandeven 1991), was used to generate the kernel. It is an example of how the filters can get better results when extra information is available.

To summarize, the 2D physical space filter is effective in the case that the peaks of the Himalayas or the steepness of the Andes is desired to be maintained or in the case that only the ocean ripples are to be suppressed.

7. Conclusions

In simulating the atmospheric circulation using spectral transform models, the Gibbs oscillation (referred to here as G bias) sometimes generates unfavorable solutions. This adverse effect is particularly pronounced in the simulated rainfall and clouds, but other variables also suffer from the G bias. However, the G bias can be substantially reduced by using filtering kernels. Some key points are reviewed below.

1) There are two areas in which the reduction of the G bias seems particularly effective. One is the specification of orography, and the other is the calculation of the condensation of water vapor.

2) Various filters are discussed and tested. Among them, the 2D isotropic filter appears favorable for use in experiments with atmospheric spectral models. This filter is based on the Cesaro summation principle with a constraint on two-dimensional wavenumber.

3) Removal of the orographic G bias significantly improves the quality of simulations. In particular, unrealistic spotty rainfall has diminished, and the rainfall distribution has become better organized. Precipitation patterns over the Sahel are greatly improved, showing increased spatial coherence. Cloud distributions are also improved, eliminating the unrealistic ripple patterns.

4) Although the 2D isotropic filter is effective as mentioned above, there is a significant reduction of high mountain peaks, such as the Himalayas, in the case of the low-resolution model. To remedy this, a 2D physical space filter is proposed, which retains the high-mountain peak values.

5) Concerning the mixing ratio of water vapor, negative values are enhanced by the G bias. In order to rectify this problem, several schemes are tested. Thus far, a selective application of the 1D Lanczos filter has been partially successful.

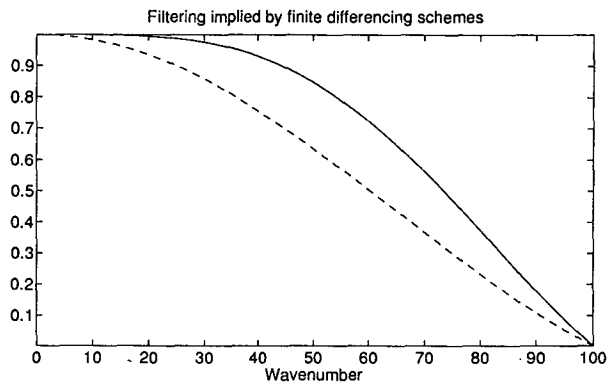

FIG. 19. Implicit filtering produced by finite-differencing schemes. The curves show the damping factor for each wavenumber implied by the discretization; a value of 1 means that no filtering is done. Second-order centered (dashed) and fourth-order (solid) differencing schemes are plotted.

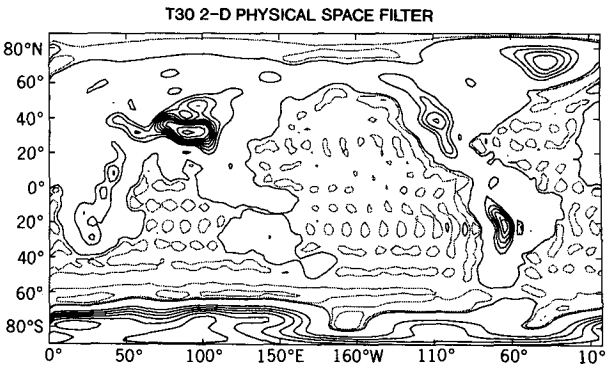

FIG. 20. Spectral orography at T30 filtered only in ocean points with the physical space filter. Contour interval is the same as in Fig. 7.

Acknowledgments. One of the authors (A. Navarra) was partially supported by the EEC contract "Climate of the XXI Century," within the EPOCH program, and by NSF Grant NA26RG0102-01. The authors would also like to thank Drs. S. Manabe and J. Mahlman for stimulating discussions, and Messrs. R. Smith, A. Rosati, R. Gudgel, and Ms. W. Marshall for invaluable assistance. Many thanks also go to A. Broccoli and J. Anderson for reading previous versions of the manuscript. The pictures were skillfully drafted by the GFDL illustration group.

REFERENCES

Bourke, W., 1972: An efficient, one level primitive equation spectral model. *Mon. Wea. Rev.*, **100**, 683–689.

Cai, W., D. Gottlieb, and C.-W. Shu, 1992: On one sided filters for spectral Fourier approximations of discontinuous functions. *SIAM J. Numer. Anal.*, **29**, 905–916.

Canuto, C., et al., 1988: *Spectral Methods in Fluid Dynamics.* Springer-Verlag, 557 pp.

Duchon, C. E., 1979: Lanczos filtering in one and two dimensions. *J. Appl. Meteor.*, **18**, 1016–1022.

Eliasen, E., B. Machenhauer, and E. Rasmussen, 1971: On a numerical method for integration of the hydrodynamical equations with a spectral representation of the horizontal fields. Report No. 2, Institute for Theoretical Meteorology, Copenhagen University, Copenhagen, Denmark, 37 pp.

Gates, W. L., and A. B. Nelson, 1975: A new (revised) tabulation of the Scripps topography on a 1° global grid. Part I: Terrain heights.

R-1276-1-ARPA, Rand Corporation, Santa Monica, CA, 132 pp. [Also available from NOAA/NESDIS, NGDC, 325 Broadway, E/CG4, Boulder, CO.]

Gordon, C. T., 1992: Comparison of 30-day integrations with and without cloud–radiation interaction. *Mon. Wea. Rev.*, **120,** 1244–1277.

——, and W. F. Stern, 1982: A description of the GFDL global spectral model. *Mon. Wea. Rev.*, **110,** 625–644.

Hogan, T. R., and T. E. Rosmond, 1991: The description of the navy operational global atmospheric prediction system's spectral forecast model. *Mon. Wea. Rev.*, **119,** 1786–1815.

Hoskins, B. J., 1980: Representation of the earth topography using spherical harmonics. *Mon. Wea. Rev.*, **108,** 111–115.

Jaeger, L., 1976: Monatskarten des Niederschlages fur die ganze Erde. *Ber. Dtsch. Wetterdienstes,* **18,**

Jenkins, G. M., and D. G. Watts, 1968: *Spectral Analysis and Its Applications.* Holden-Day, 525 pp.

Korner, T. W., 1990: *Fourier Analysis.* Cambridge University Press, 591 pp.

Lanczos, C., 1956: *Applied Analysis.* Prentice-Hall, 539 pp.

Manabe, S., J. Smagorinsky, and R. F. Strickler, 1965: Simulated climatology of a general circulation model with a hydrological cycle. *Mon. Wea. Rev.*, **93,** 769–798.

Miyakoda, K., A. Rosati, and R. Gudgel, 1993: Toward the GCM El Niño simulation. *Proc. of NATO Advanced Research Workshop on Prediction of Interannual Climate Variations,* 125–152.

Orszag, S. A., 1970: Transform method for the calculation of vector-coupled sum application to the spectral form of the vorticity equation. *J. Atmos. Sci.*, **27,** 890–895.

Sardeshmukh, P. D., and B. J. Hoskins, 1984: Spatial smoothing on the sphere. *Mon. Wea. Rev.*, **112,** 2524–2529.

Schubert, S., C.-K. Park, W. Higgins, S. Moorthi, and M. Suarez, 1990: An atlas of ECMWF analyses (1980–87). Part I—First moment quantities: NASA Tech. Memo. 100747, Goddard Space Flight Center, Greenbelt, MD, 258 pp.

Stern, W. F., and K. Miyakoda, 1989: Systematic errors in GFDL's extended range prediction spectral GCM. *Proc. Workshop on Systematic Errors in Models of the Atmosphere,* WMO, 136–140.

——, and ——, 1991: The feasibility of seasonal NWP from decadal simulations. *Proc. Ninth Conf. on Numerical Weather Prediction,* Denver, CO, Amer. Meteor. Soc., 649–651.

Thompson, P. D., 1956: Optimum smoothing of two-dimensional fields. *Tellus,* **3,** 384–393.

Vandeven, H., 1991: Family of spectral filters for discontinuous problems. *J. Sci. Comput.*, **8,** 159–192.